Slow rupture and weakly pressure-sensitive strength enables compressional branching: Dynamic rupture simulations of the 2012 Off-Sumatra earthquake

Lingsen Meng* and Jean-Paul Ampuero

Seismological Laboratory, California Institute of Technology

*lsmeng@gps.caltech.edu
California Institute of Technology
Seismological Laboratory
1200 E. California Blvd., MS 252-21
South Mudd Building, Room 364
Pasadena, CA 91125
Phone: (626) 395-6931
Fax: (626) 564-0715

Abstract:

The 2012 M8.6 off-Sumatra earthquake, the largest strike-slip and intraplate earthquake recorded to date, followed an exceptionally tortuous rupture path. It featured two episodes of branching into fault segments that were experiencing increased compressive dynamic stresses, hence increased frictional strength. Meng et al. (2012) attributed this unexpected compressional branching to slow rupture and weak pressure-sensitivity of the fault strength. Here, by conducting 2D dynamic rupture simulations, we confirm that the compressional branching can only occur under slow rupture speed and low apparent friction coefficient. Poroelastic effects can also contribute by buffering the dynamic clamping. We suggest that serpentinized minerals may provide low friction, fluids and dynamic weakening down to 25 km depth, and ductile shear heating instability may provide a weakening mechanism from 40 to 60 km depth. The absence of known weakening mechanism in the intermediate depth range suggests that rupture may penetrate over velocity-strengthening regions.

Introduction:

The possibility of an earthquake rupture propagating along distinct branches of a fault system has been the subject of several earthquake dynamic studies. Understanding the mechanics of fault branching, rupture path selection and the connectivity of rupture across multiple fault segments could provide a physical basis to assess the maximum earthquake size in complex fault systems. The basic principles of rupture branching are established based on analytical studies. [Poliakov et al., 2002; Kame et al., 2003] show that fault branching can occur under specific conditions of principal stress orientation, branching angles and rupture speed. On the other hand, rupture branching can be complicated by the interaction with directivity effects [Fliss et al, 2005], rupture propagation and arrest [Bhat et al, 2005], heterogeneous stress distribution and state in the earthquake cycle [Duan and Oglesby, 2007]. The 2012 M8.6 off-Sumatra earthquake provides a rare example of large scale branching in a system of almost orthogonal faults [Meng et al., 2012]. Its rupture path showed preferred branching into the compressional side, i.e. into faults that were experiencing increased normal stresses. This challenges the conventional view that clamping increases frictional strength and hence discourages compressional branching [Oglesby, 2005]. Meng et al. (2012) attributed this puzzling observation to weak pressure-sensitivity of fault strength (low apparent friction coefficient) in the deep oceanic lithosphere. Recent opportunities and advances in observation studies of large megathrust earthquakes, especially the 2011 M9.0 Tohoku-Oki event, based on space-geodesy [Ozawa et al., 2011; Simons et al., 2011], waveform inversions [Ide et al.,2011; Wei et al., 2012] and short-period back-projections [Ishii et al., 2011; Koper et al., 2011; Meng et al., 2011] have facilitated numerous efforts to understand the underlying earthquake physics through dynamic simulations, assessing the role of a variety of ingredients, including depth-dependent heterogeneities [Huang et al., 2012; Kato et al., 2011], plastic dissipation and poroelasticity [Ma et al., 2012], subducting seamounts [Duan et al.,2012] and shallow velocity-strengthening [Kozdon and Dunham et al., 2012]. The unusual complexity of the 2012 off-Sumatra event, the largest strike-slip and intraplate earthquake recorded to date, provides an opportunity to shed light on the dynamics of such extreme events. Here, we conduct dynamic rupture simulations to address the conditions on friction, rupture speed, stress drop and poroelastic properties that allow dynamic branching on an orthogonal segment in a compressional quadrant.

Observations and their uncertainty:

The fault geometry and the rupture process of this event are constrained essentially by teleseismic back-projection studies. Meng et al. (2012) described its complicated rupture path, involving multiple segments of a network of orthogonal conjugate faults, and branching twice into dynamically clamped fault segments (Figure 1). In the first compressional branching episode, when rupture on the right-lateral fault A (NW-SE oriented) reached the orthogonal left-lateral fault B (NE-SW oriented), the SW branch of fault B instantaneously started breaking, while the rupture on the NE branch was delayed by about 15 s. Later, the SW-ward rupture on fault B branched into the NW segment of the orthogonal fault C, which is again on the compressional quadrant. Here, to determine the possible range of the dynamic rupture model parameters, we quantify the uncertainty of the fault bisecting angle, the rupture speed and the mean stress drop.

The aftershocks and back-projection source imaging suggest a system of almost orthogonal faults. The two dominant orientations of the fault system are best delineated by the back-projection results of the mainshock rupture on fault C and of the M8.2 aftershock rupture (Figure 1). By linear-fitting the strike of the corresponding faults, we obtained the bisecting angle of 87 +- 3 °. We also estimate the rupture speed prior to the compressional branching episodes, on the NW branch of fault A and on the SW branch of fault B. The rupture initiates rather slowly on fault A with 29% (25%~33%) of the shear wave speed at the centroid depth of 30 km in the uppermost mantle (4.6 km/s, Klingelhoefer et al). The SW rupture on fault B propagates with 55% (50%~60%) of the shear wave speed. The stress drop is the quantity least constrained by the current observations, because of large uncertainties on the depth extent of the rupture. The overall mean stress drop can be estimated as $\Delta\tau = M_0/(\pi W^2 L)$ (Leonard et al, 2010). Given the seismic moment of $M_0 = 10^{22}$ Nm (USGS) and rupture length L = 400 km (the combined length of faults A and B, where most of the moment was released), the estimated stress drop is $\Delta\tau$ = 2.2 MPa if we assume the depth range W = 60 km, twice the centroid depth [Duputel et al., 2012]. If we assume the depth range of significant slip is W = 30 km, half of the above estimate, the resulting stress drop is 8.8 MPa. However, the stress drop can be highly spatially variable. On fault A it can be as large as 17.6 MPa given half of the total moment is released there on a 100 km long rupture.

Model setup and assumptions:

We develop a 2D dynamic rupture model of compressive branching during the off-Sumatra earthquake. The model comprises a T-shaped fault system with an initial fault **a** and an orthogonal fault **b**. The 2D model plane represents a cross-section of the crust at fixed depth. The mid-point of fault **b** is connected with one end of fault **a**. Both faults are 200 km long and embedded in a homogeneous rectangular elastic space with absorbing boundaries. Both faults are optimally oriented with respect to the regional stress (45 ° to the principal stress axis, based on Delescluse et al, 2007). The dynamic rupture simulation is solved with the spectral element code SEM2DPACK (http://www.sourceforge.net/projects/sem2d/). The assumed density, P and S wave velocities are 3000 km/m3, 8000 m/s and 4618 m/s, respectively.
The rupture is set to nucleate at the midpoint of fault **a**. The fault is governed by the linear slip-weakening friction law. Based on an analytical solution for the dynamic Coulomb stress at the tip

of a propagating crack [Poliakov et al., 2002; Freund, 1998], Meng et al. (2012) found that compressional branching is permitted only with low rupture speed and low friction coefficient. (We note that low friction, if accompanied by large cohesion, does not imply low absolute strength.) To confirm this interpretation, we model four different situtations: 1: slow and pressure-insensitive (zero friction with cohesion and low rupture speed), 2: slow and weakly pressure-sensitive (low friction and low rupture speed), 3: fast and weakly pressure-sensitive (low friction and high rupture speed), 4: slow and strongly pressure-sensitive (high friction and low rupture speed). The pressure sensitivity is controlled by the friction coefficient. The slow rupture speed can result from self-similar energy dissipation, for instance due to non-elastic off-fault deformation [Andrews, 2005]. In an elastic model, this process can be mimicked by slip-weakening friction by setting a non-uniform critical slip distance *Dc* that grows linearly away from the hypocenter. The rupture speed V_r is related to other model parameters by [Andrews et al., 2005; Kikuchi et al., 1975]

$$1 - \frac{V_r}{V_R} \sim \frac{G\sigma_n \Delta\mu D_c'}{\Delta\tau^2}$$

where V_R is the Rayleigh wave speed, *G* is shear modulus, $\Delta\tau$ is the stress drop, σ_n is the normal stress, $\Delta\mu$ is the friction drop and *Dc'* is the spatial gradient of *Dc*. The stress drop is set to 13 MPa, the average of our high and low stress drop estimates. The sketch of each model is shown in figure 2 and the parameters are listed in table 1. In this study, we focus on the failure condition of fault **bc** (the compressional branch). Therefore, since fault **bd** (the dilatational branch) is always favored to break by the dynamic Coulomb stress, we lock the fault **bd** to avoid triggering of **bc** by **bd** (Figure S1). We also locked the junction between faults **a** and **b**, since this particular point always has zero dynamic stress for perfectly orthogonal faults. In reality, a slightly oblique angle results in nonzero dynamic stress at the junction. Finally, we lock the last 10 km of fault **a** close to the boundary to avoid the artificial large slip and reflection phase.

Results:

The spatio-temporal distributions of slip rate resulting from our simulations are shown in Figure 3. In all the models, the rupture propagated bilaterally along fault **a** and accelerated to steady-state speeds. In the 'fast' case with small but non-zero gradient of *Dc* (model 3), the rupture reaches the Rayleigh wave speed (~4 km/s). The slip rate function shows crack-like behaviour with peak value following closely the leading rupture front. In contrast, in the 'slow' case the relatively large gradient of *Dc* creates self-similar cracks with large process zone, which broadens with rupture propagation distance. In models 1, 2 and 4, the peak slip velocity, which we associate to the high frequency radiation imaged by our back-projection study, propagates at a significantly slow speed, 55% percent of the shear wave speed (~2.5 km/s), similar to the observed value on fault B (Figure 1). In all the four models, the rupture reached the junction of faults **a** and **b**. However, the branching behaviours are rather different. Models 1 and 2 are set up with the same rupture speed and static strength through cohesion or low friction (Figure 3-inset). Fault **bc** in Model 1 instantaneously breaks when the rupture reaches the junction while the branching in Model 2 is delayed due to non-zero compressional stress. On the other hand, Models 3 and 4 fail to break fault **bc**. The large peak slip velocity due to either large rupture speed or large friction (and proportionally large friction drop) generates a larger compressional dynamic stress field that prohibits branching. These simulations demonstrate that low rupture speed and low apparent friction are prerequisites for dynamic compressional branching. These results are stable within the range of uncertainty on stress drop and rupture speed. A set of models with slower rupture speed (30% V_s) and larger stress drop (17 Mpa) observed on fault A are shown in Figure S2.

Another factor that can potentially facilitate compressional branching is the poroelastic effect. In a 2D linear poroelastic medium, the effective normal stress σ_e is:

$$\sigma_e = \sigma_n - \sigma_p = \sigma_n - \frac{2B(1+\vartheta)}{3} \cdot \frac{\sigma_{xx} + \sigma_{yy}}{2}$$

where σ_n is the normal stress, σ_p is pore pressure, σ_{xx} and σ_{yy} are the stresses in the 2D x-y plane, ϑ is Poisson's ratio (set to 0.25) and B is the Skempton coefficient, defined as the ratio of pore pressure change and the mean stress change. The above analysis only provides necessary conditions on friction and rupture speed to break fault **bc**, but it does not explain why the preferred branching direction is towards the compressive side. [Viesca et al., 2008; Ma, 2012] show that if the regional maximum principal stress bisect the fault plane x with a small angle (such as low angle thrust faults), σ_{xx} is much larger than σ_{yy}, the normal stress σ_n (~σ_{yy}) is much smaller than the mean stress (σ_{xx} + σ_{yy})/2, and a large Skempton coefficient results in high pore pressure larger than the normal stress. Therefore the effective normal stress change is negative and failure is promoted on the compressional side (Figure 4 in Viesca et al). However, in the case of the off-Sumatra earthquake, the maximum principal stress bisects the faults at 45 °, which means $\sigma_{xx} \sim \sigma_{yy}$, therefore the mean stress is similar to the normal stress. The effective normal stress remains positive for reasonable values of the Skempton coefficient $B \sim 0.5$. The poroelastic effect limits the mean stress changes (Coulomb stress increases on the compressional side and decreases on the dilatational side) and equalizes the probability of branching on both sides, but it does not favour the compressional branch. The preferred compressional branching might involve geometrical complexities and heterogeneous stress distribution that cannot be resolved by current observations. Nevertheless, even moderate Skempton coefficients (B ~ 0.5) relax the requirements for compressional branching by permitting positive Coulomb stress changes at larger friction coefficients (Figure 4). In laboratory experiments, high Skempton coefficients (B ~ 1) are observed at low effective confining stress [Paterson and Wong, 2005]. Given that the strength drop (the product of effective normal stress and the static to dynamic friction coefficient drop) is greater than the stress drop, $\Delta\mu \cdot \sigma_e > \Delta\tau \sim 13\ MPa$, the effective normal stress σ_e is larger than 26 MPa even assuming a large friction drop $\Delta\mu$ = 0.5. Based on the laboratory data summarized by [Paterson and Wong, 2005], the corresponding Skempton coefficient is limited to B <= 0.5.

Discussion:

We showed that compressional branching in almost orthogonal conjugate faults requires low friction coefficient and slow rupture speed, and is aided by the presence of fluids (poroelastic effect). However, the origin of low friction and the source of fluids remain to be identified. Meng et al. (2012) discussed a possible petrological origin of low friction based on serpentinization in the Indian ocean lithosphere [Delescluse and Chamot-Rooke, 2007]. Serpentine is found to have low friction coefficient in laboratory experiments [Escartin et al., 2001]. The dehydration embrittlement of the serpentine minerals due to shear heating can provide fluids and a weakening mechanism at depth [Jung et al., 2004]. The serpentine mineral antigorite is stable up to ~720 ° C and 2 GPa [Ulmer and Trommsdorff, 1995], which corresponds to about 40 km depth in our context. However, the serpentinization reaction is possible only up to 400-500 ° C, which corresponds to about 25 km depth [Delescluse and Chamot-Rooke, 2008]. The serpentinization might interact with downward fault growth through multiple earthquake cycles. These earthquakes are further facilitated by serpentinization and also create channels for deeper infiltration of fluids. The fault system is probably systematically activated by the megathrust earthquakes in the Sunda subduction zone, such as the 2004 Sumatra event. The centroid depth of the earthquake is around 30 km, implying that the rupture extends even deeper than 25 km, beyond the maximum depth where the serpentinization reaction is possible. The ductile shear heating instability [Kelemen and Hirth, 2007; McGuire and Beroza, 2012] operating between 40 and 60 km depth provides a weakening mechanism to explain the deeper slip. The gap between 25 and 40 km might be a frictionally stable region dragged along by the shallower and/or deeper rupture. Hillers et al. (2006) showed that ruptures can penetrate well beneath the nominal seismogenic layer into velocity-strengthening regions.

Our study highlights that the connectivity of rupture across multiple fault segments is a key factor of earthquake hazard. While the odds of a rupture involving multiple fault segments decreases quickly with the number of segments [Wesnousky et al., 2011], these extreme events often surprise us in most unexpected ways and places and cause the most significant damage. More efforts on estimating the possibility of earthquakes connecting segments are certainly needed in places like the San Andreas and New Madrid fault system. Finally, this work demonstrates the importance of having fine observations to constrain earthquake source dynamics studies. Particularly, back-projection studies of recent large earthquakes demonstrate that large scale arrays need to be maintained to image future large earthquakes. The Earthscope

Global Array of BroadBand Arrays (GABBA) initiative is one such effort to continue the source imaging capability beyond the end of the USArray project.

Reference:

Andrews, D. J. (2005), Rupture dynamics with energy loss outside the slip zone, J Geophys Res-Sol Ea, 110(B1).

Bhat, H. S., M. Olives, R. Dmowska, and J. R. Rice (2007), Role of fault branches in earthquake rupture dynamics, J Geophys Res-Sol Ea, 112(B11).

Delescluse, M., and N. Chamotrooke (2007), Instantaneous deformation and kinematics of the India-Australia Plate, Geophys J Int, 168(2), 818-842.

Delescluse, M., and N. Chamot-Rooke (2008), Serpentinization pulse in the actively deforming Central Indian Basin, Earth Planet Sc Lett, 276(1-2), 140-151.

Duan, B., and D. D. Oglesby (2007), Nonuniform prestress from prior earthquakes and the effect on dynamics of branched fault systems, J Geophys Res-Sol Ea, 112(B5).

Duan, B. C. (2012), Dynamic rupture of the 2011 Mw 9.0 Tohoku-Oki earthquake: Roles of a possible subducting seamount, J Geophys Res-Sol Ea, 117.

Duputel, Z., H. Kanamori, V. Tsai., L. Rivera., L. Meng., and J.-P. Ampuero (2012), The 2012 Sumatra great earthquake sequence, in preparation.

Escartin, J., G. Hirth, and B. Evans (2001), Strength of slightly serpentinized peridotites: Implications for the tectonics of oceanic lithosphere, Geology, 29(11), 1023-1026.

Fliss, S., H. S. Bhat, R. Dmowska, and J. R. Rice (2005), Fault branching and rupture directivity, J Geophys Res-Sol Ea, 110(B6).

Freund, L. B. (1998), Dynamic Fracture Mechanics, Cambridge University Press, 563.

Hillers, G., Y. Ben-Zion, and P. M. Mai (2006), Seismicity on a fault controlled by rate- and state-dependent friction with spatial variations of the critical slip distance, J Geophys Res-Sol Ea, 111(B1).

Huang, Y., L. Meng, and J.-P. Ampuero (2012), A Dynamic Model of the Frequency-Dependent Rupture Process of the 2011 Tohoku-Oki Earthquake, Earth Planets Space (speical issue on the Tohoku earthquake), In press.

Ide, S., A. Baltay, and G. C. Beroza (2011), Shallow Dynamic Overshoot and Energetic Deep Rupture in the 2011 M-w 9.0 Tohoku-Oki Earthquake, Science, 332(6036), 1426-1429.

Ishii, M. (2011), High-frequency rupture properties of the M-w 9.0 off the Pacific coast of Tohoku Earthquake, Earth Planets Space, 63(7), 609-614.

Jung, H., H. W. Green, and L. F. Dobrzhinetskaya (2004), Intermediate-depth earthquake faulting by dehydration embrittlement with negative volume change, Nature, 428(6982), 545-549.

Kame, N., J. R. Rice, and R. Dmowska (2003), Effects of prestress state and rupture velocity on dynamic fault branching, J Geophys Res-Sol Ea, 108(B5).

Kato, N., and S. Yoshida (2011), A shallow strong patch model for the 2011 great Tohoku-oki earthquake: A numerical simulation, Geophys Res Lett, 38.

Kelemen, P. B., and G. Hirth (2007), A periodic shear-heating mechanism for intermediate-depth earthquakes in the mantle, Nature, 446(7137), 787-790.

Kikuchi, M. (1975), Inelastic effect on crack propagation, J. Phys. Earth(23).

Klingelhoefer, F., M. A. Gutscher, S. Ladage, J. X. Dessa, D. Graindorge, D. Franke, C. Andre, H. Permana, T. Yudistira, and A. Chauhan (2010), Limits of the seismogenic zone in the epicentral region of the 26 December 2004 great Sumatra-Andaman earthquake: Results from seismic refraction and wide-angle reflection surveys and thermal modeling, J Geophys Res-Sol Ea, 115.

Koper, K. D., A. R. Hutko, and T. Lay (2011), Along-dip variation of teleseismic short-period radiation from the 11 March 2011 Tohoku earthquake (M-w 9.0), Geophys Res Lett, 38.

Kozdon, J., and E. Dunham (2012), Rupture to the trench: Dynamic rupture simulations of the 11 March 2011 Tohoku earthquake, B Seismol Soc Am, submitted.

Leonard, M. (2010), Earthquake Fault Scaling: Self-Consistent Relating of Rupture Length, Width, Average Displacement, and Moment Release, B Seismol Soc Am, 100(5A), 1971-1988.

Ma, S. (2012), A self-consistent mechanism for slow dynamic deformation and tsunami generation for earthquakes in the shallow subduction zone, Geophys Res Lett, 39.

McGuire, J., and G. C. Beroza (2012), A Rogue Earthquake Off Sumatra, Science, 336(6085).

Meng, L., A. Inbal, and J. P. Ampuero (2011), A window into the complexity of the dynamic rupture of the 2011 Mw 9 Tohoku-Oki earthquake, Geophys Res Lett, 38.

Meng, L., J. P. Ampuero, J. Stock, Z. Duputel, Y. Luo, and V. C. Tsai (2012), An earthquake in a maze: compressional rupture branching during the 11 April 2012 M8.6 off-Sumatra earthquake, Science, In press.

Oglesby, D. D. (2005), The dynamics of strike-slip step-overs with linking dip-slip faults, B Seismol Soc Am, 95(5), 1604-1622.

Ozawa, S., T. Nishimura, H. Suito, T. Kobayashi, M. Tobita, and T. Imakiire (2011), Coseismic and postseismic slip of the 2011 magnitude-9 Tohoku-Oki earthquake, Nature, 475(7356), 373-U123.

Paterson, M. S., and T.-F. Wong (2005), Experimental Rock Deformation - The Brittle Field, 358 pp., Springer.

Poliakov, A. N. B., R. Dmowska, and J. R. Rice (2002), Dynamic shear rupture interactions with fault bends and off-axis secondary faulting, J Geophys Res-Sol Ea, 107(B11).

Simons, M., et al. (2011), The 2011 Magnitude 9.0 Tohoku-Oki Earthquake: Mosaicking the Megathrust from Seconds to Centuries, Science, 332(6036), 1421-1425.

Ulmer, P., and V. Trommsdorff (1995), Serpentine Stability to Mantle Depths and Subduction-Related Magmatism, Science, 268(5212), 858-861.

Viesca, R. C., E. L. Templeton, and J. R. Rice (2008), Off-fault plasticity and earthquake rupture dynamics: 2. Effects of fluid saturation, J Geophys Res-Sol Ea, 113(B9).

Wei, S., S. Helmberger, J.-P. Avouac, and J. L. Jiang (2011), Sources of shaking and flooding by the Tohoku-Oki Earthquake, a case for thermal pressurization, Earth Planet Sc Lett, submitted.

Wesnousky, S. G., and G. P. Biasi (2011), The Length to Which an Earthquake Will Go to Rupture, B Seismol Soc Am, 101(4), 1948-1950.

Acknowledgement:

This research was supported by NSF grant EAR-1015704, by the Gordon and Betty Moore Foundation and by the Southern California Earthquake Center, which is funded by NSF Cooperative Agreement EAR-0106924 and USGS Cooperative Agreement 02HQAG0008. The broadband seismogram from Japanese Hi-net (www.hinet.bosai.go.jp) and the European ORFEUS center (www.orfeus-eu.org) were used to conduct the back-projections. We thank Victor Tsai, Shiqing Xu and Yihe Huang for valuable discussions. This paper is Caltech Tectonics Observatory contribution #XXX and Caltech Seismo Lab contribution #XXX.

Figure Caption:

Figure 1: Uncertainty of the bisecting angle of the conjugate fault system (left) and the rupture speed (right) inferred from teleseismic back-projection source imaging. Left: the dark grey (mainshock) and light grey (M8.2 aftershock) circles indicate the positions of high-frequency radiation imaged with the Japanese Hi-net network. Their size is scaled by the beamforming amplitude. Black dots are the epicenters of the first day of aftershocks from the NEIC catalog. The black rectangles denotes the fault plane A, B and C of the M8.6 mainshock and the fault plane of the M8.2 aftershock. The dashed lines are the linear-fit fault planes of the M8.2 aftershock and the late NW-ward rupture of the mainshock. The bisecting angle is 87 ° (84~90 °) based on one sigma variance of each fault plane. Right: The high frequency radiators imaged with European (circles) and Japanese (squares) networks as a function of distance along the rupture path (positive NW-ward on faults A and C, and SW-ward on fault B) and rupture time. The ratio of rupture speed to shear wave speed (4.6 km/s) along the NW branch of fault A and SW branch of fault B is 29% (25%~33%) and 55% (50%~60%), respectively.

Figure 2: Sketch of the simulation setup. The yellow, blue and grey lines denote the initial right lateral fault **a** and the orthogonal branching fault segments **bc** (compressional) and **bd** (dilatational). The faults are embedded in a homogeneous elastic medium surrounded by absorbing boundaries. The red star is the hypocenter.

Figure 3: Spatio-temporal distribution of slip rate on the initial fault **a** and branching fault **b** for various models. a: slow and pressure insensitive, b: slow and weakly pressure sensitive, c: fast

and weakly pressure sensitive, d: slow and strongly pressure sensitive. Insets in bottom plots show the failure envelope in shear strength (τ) vs. normal stress (σ) diagrams of the four models with different friction coefficient mu, cohesion C and rupture speed Vr.

Figure 4: Maximum friction coefficient (μ) that allows compressive branching (positive dynamic Coulomb stress change near the rupture tip), as a function of rupture speed (Vr) and for three values of the Skempton coefficient B (see legend). The curves correspond to branching on an orthogonal fault, and the color bands encompass the range of fault orientations within the uncertainty inferred from the back-projection results (Figure 1). This analysis is based on analytical solutions for the dynamic stresses near a propagating rupture front (Poliakov et al, 2002). The numbers in circles indicate the parameters settings of the dynamic rupture models (with B = 0) shown in Figure 3, which confirm these analytical arguments.

Table 1: Parameters of the four models shown in Figure 3

Model index	μ_s	μ_d	C	σ_0	τ_0	Vr/Vs	$\Delta\tau$	*Dc'*
1	0	0	38 Mpa	250 Mpa	38 Mpa	0.54	13 Mpa	2.2×10^{-3}
2	0.2	0.1	0	250 Mpa	38 Mpa	0.54	13 Mpa	2.2×10^{-3}
3	0.2	0.1	0	250 Mpa	38 Mpa	0.89	13 Mpa	6×10^{-4}
4	0.6	0.4	0	250 Mpa	115 Mpa	0.54	15 Mpa	1.5×10^{-3}

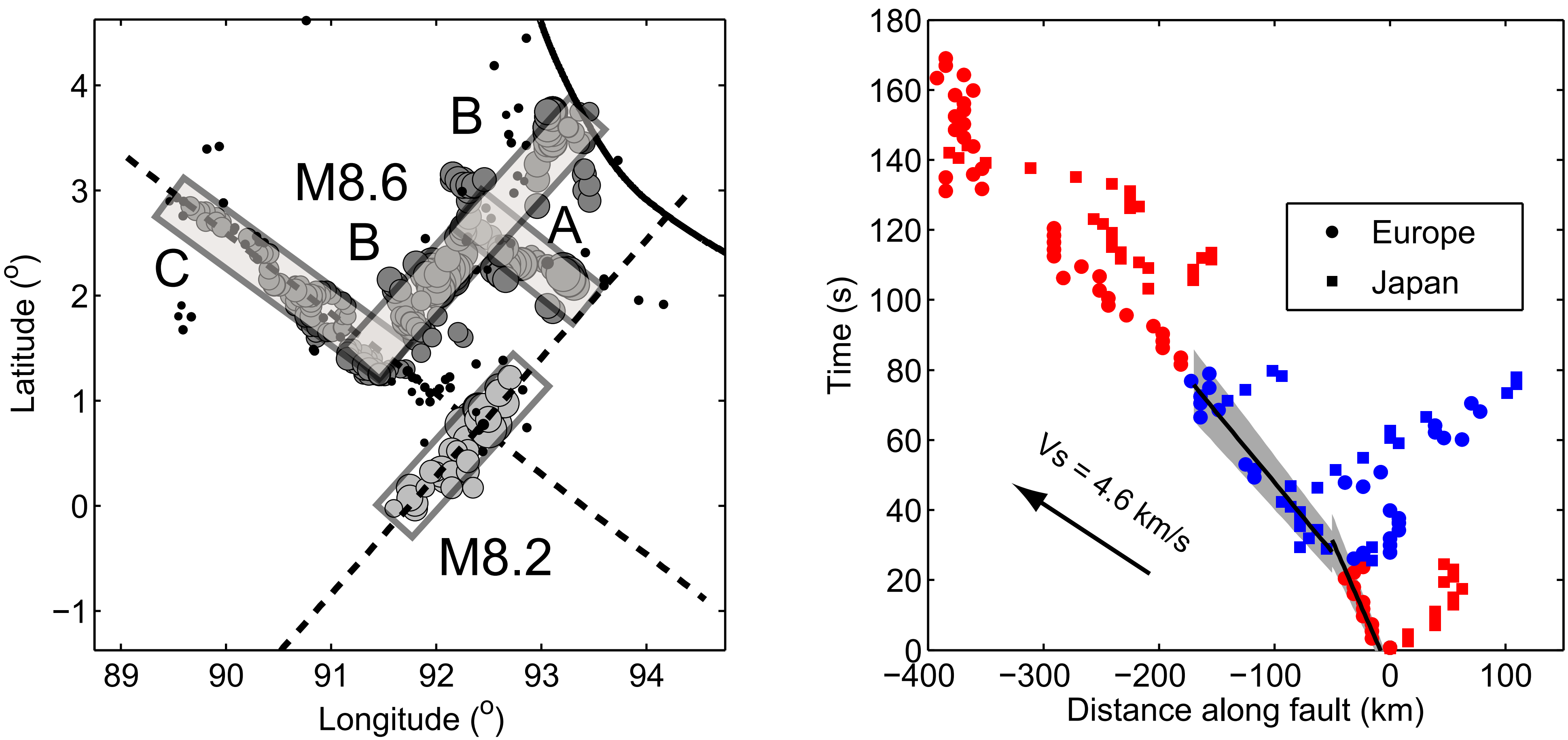

Latitude (°)
Longitude (°)
M8.6
M8.2
A
B
B
C
Time (s)
Distance along fault (km)
Europe
Japan
Vs = 4.6 km/s

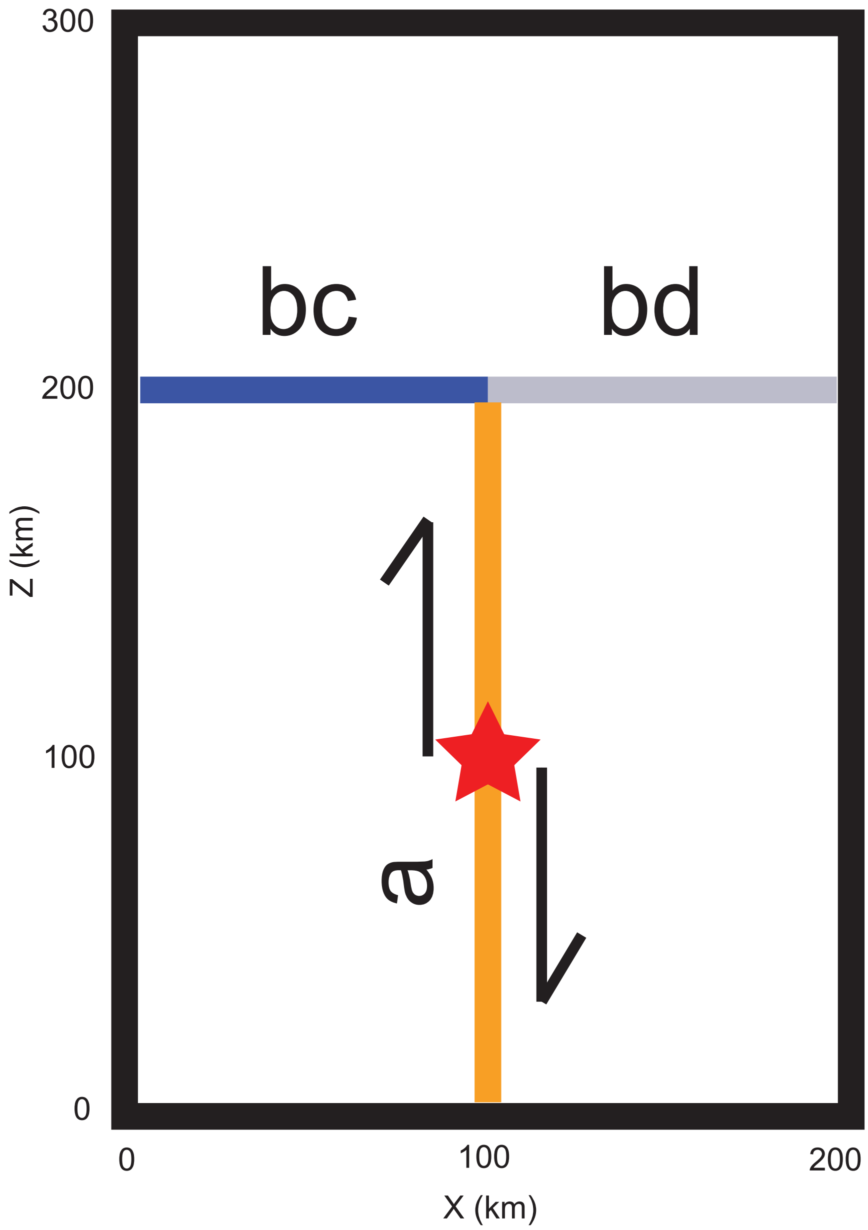
300
bc
bd
200
Z (km)
100
a
0
0
100
200
X (km)

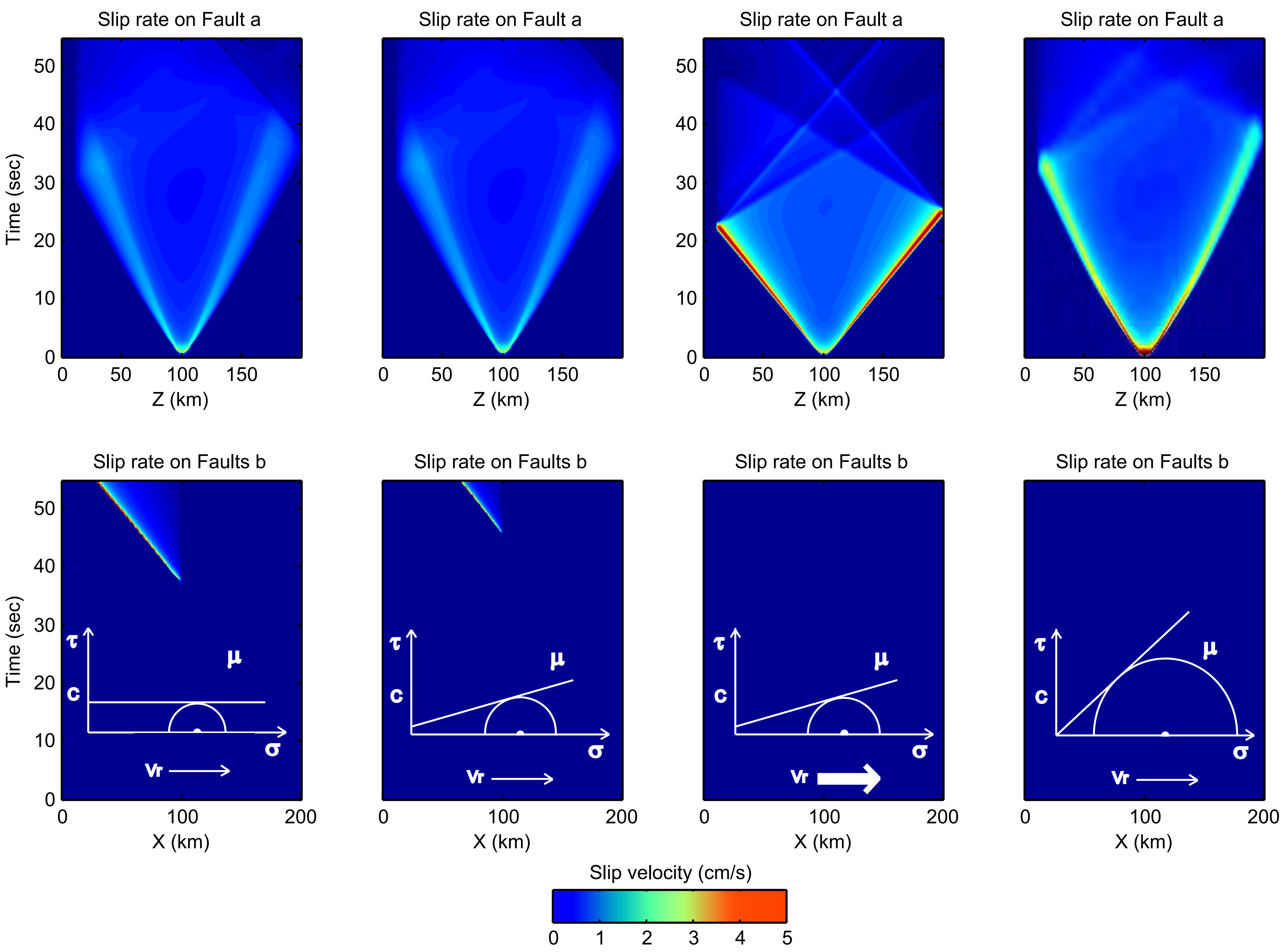

Slip rate on Fault a
Slip rate on Fault a
Slip rate on Fault a
Slip rate on Fault a
Time (sec)
Z (km)
Slip rate on Faults b
Slip rate on Faults b
Slip rate on Faults b
Slip rate on Faults b
Time (sec)
X (km)
τ
c
μ
σ
Vr
Slip velocity (cm/s)
0 1 2 3 4 5

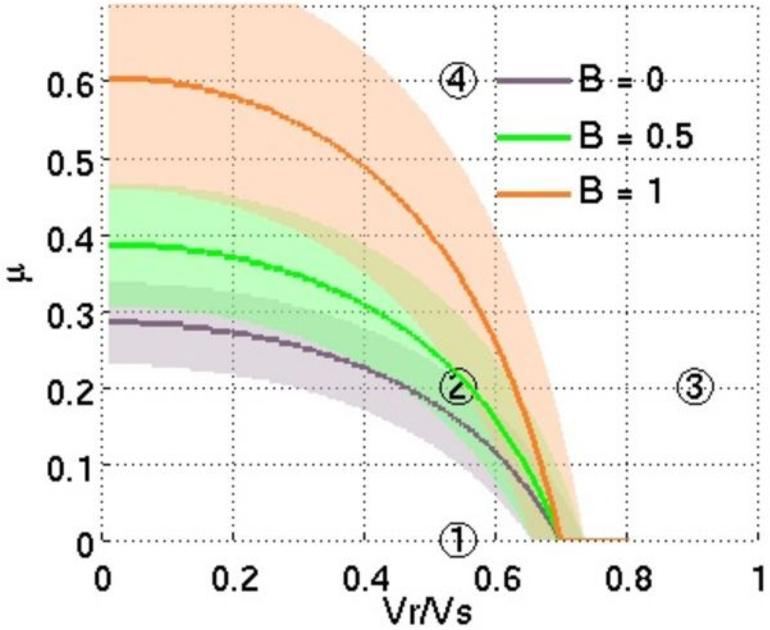

0.6
0.5
0.4
0.3
0.2
0.1
0
μ
0
0.2
0.4
0.6
0.8
1
Vr/Vs
B = 0
B = 0.5
B = 1
④
②
③
①

Model index	μ_s	μ_d	C	σ_0	τ_0	Vr/Vs	$\Delta\tau$	*Dc'*
1	0	0	38 Mpa	250 Mpa	38 Mpa	0.54	13 Mpa	2.2×10^{-3}
2	0.2	0.1	0	250 Mpa	38 Mpa	0.54	13 Mpa	2.2×10^{-3}
3	0.2	0.1	0	250 Mpa	38 Mpa	0.89	13 Mpa	6×10^{-4}
4	0.6	0.4	0	250 Mpa	115 Mpa	0.54	15 Mpa	1.5×10^{-3}